

IFCPT S-Duct Grid-Adapted FUN3D Computations for the Third Propulsion Aerodynamics Workshop

Zach S. Davis*

Pointwise, Inc., Fort Worth, TX 76104, USA

M. A. Park†

NASA Langley Research Center, Hampton, VA 23681-2199, USA

Contributions of the unstructured Reynolds-averaged Navier-Stokes code, FUN3D, to the 3rd AIAA Propulsion Aerodynamics Workshop are described for the diffusing IFCPT S-Duct. Using workshop-supplied grids, results for the baseline S-Duct, baseline S-Duct with Aerodynamic Interface Plane (AIP) rake hardware, and baseline S-Duct with flow control devices are compared with experimental data and results computed with output-based, off-body grid adaptation in FUN3D. Due to the absence of influential geometry components, total pressure recovery is overpredicted on the baseline S-Duct and S-Duct with flow control vanes when compared to experimental values. An estimate for the exact value of total pressure recovery is derived for these cases given an infinitely refined mesh. When results from output-based mesh adaptation are compared with those computed on workshop-supplied grids, a considerable improvement in predicting total pressure recovery is observed. By including more representative geometry, output-based mesh adaptation compares very favorably with experimental data in terms of predicting the total pressure recovery cost-function; whereas, results computed using the workshop-supplied grids are underpredicted.

Nomenclature

A_2	Cross-sectional area at AIP
D	AIP diameter
M_2	Mach number at AIP
N	Number of nodes in a given mesh
$P_{2_{avg}}$	Average of 8 AIP static tap pressures
$P_{T2_{avg}}$	Average of 40 AIP Kulite [®] total pressures
R	Universal gas constant
T_{T0}	Tunnel total temperature
W_2	Calculated mass flow rate at AIP
Δs	Distance measured between neighboring grid points
γ	Ratio of specific heats
L/D	S-Duct length to AIP diameter ratio
P_{T2}/P_{T0}	Ratio of total pressure at AIP to freestream total pressure
y^+	Dimensionless distance from wall boundaries
DPCP	Circumferential distortion intensity
DPRP	Radial distortion intensity

*Senior Engineer, 213 South Jennings Avenue, Fort Worth, TX 76104, AIAA Member.

†Research Scientist, Computational Aerosciences Branch, Senior Member AIAA.

PAV	Average ring pressure
PAVLOW	Average low pressure

Abbreviations

AIP	Aerodynamic Interface Plane
AMR	Adaptive Mesh Refinement
GCR	Generalized Conjugate Residual
IML	Inner Mold Line
MFP	Mass Flow Plug
PAW03	3 rd Propulsion Aerodynamics Workshop
RPM	Revolutions Per Minute

I. Introduction

THE 3rd AIAA 3rd Propulsion Aerodynamics Workshop (PAW03) preceded the 52nd AIAA/SAE/ASME Joint Propulsion Conference hosted in Salt Lake City, UT in July 2016.¹ The workshop is organized by the AIAA Air-Breathing Propulsion System Integration Technical Committee. As with earlier workshops,²⁻⁵ its primary focus is on assessing the accuracy of existing computer codes and modeling strategies in simulating unsteady and steady-state aerodynamics of complex inlet and nozzle exhaust flows of interest to the propulsion community. The workshop provides an impartial forum to present numerical results with measured empirical data for benchmark inlet and nozzle cases, exchange ideas, and evaluate the effectiveness of CFD codes and modeling techniques.

In the workshop, flow through a diffusing serpentine inlet was analyzed. Eight participants submitted datasets comprising three separate inlet configurations and a set of four flow conditions. Results submitted include 77 baseline S-Duct, 29 S-Duct with Aerodynamic Interface Plane (AIP) instrumentation, and 43 S-Duct with flow control devices modeled. An overview and summary of the workshop is given by Winkler and Davis.⁶

Workshop participants quantified S-Duct results in terms of total pressure recovery, P_{T2}/P_{T0} , as well as steady-state and dynamic distortion.⁷ When compared to experimental data, preliminary results collected from participants showed a nontrivial amount of scatter. For example, total pressure recovery values collected from workshop participants showed a 3% spread in values reported despite participants using the same set of computational grids. Results showed that the presence of the AIP rake assembly significantly influenced the flow field, but there remains some unresolved issues as to where and how the flow field should be surveyed. In other words, accurate numerical prediction of total pressure for these realistic diffusing S-Duct internal flows continues to be a challenge for computational fluid dynamics (CFD). Many factors are necessary for a CFD calculation to reliably predict such flows including accurate representation of the geometry, sufficient grid resolution, and proper turbulence modeling.

This paper describes the basic contributions of the NASA FUN3D solver⁸ to PAW03 for the diffusing S-Duct. The principal results were similar to other workshop contributions and do not add any further insights beyond what was learned at the workshop collectively. Therefore, this work examines the effect of output-based, off-body grid adaptation applied to the S-Duct as this technique is believed to be an important enabler for improved CFD predictions. This paper is organized as follows. The FUN3D solver is described first. Then output-based grid adaptation as implemented in FUN3D is outlined. The PAW03 cases are summarized in Section IV, and results are included in Section V. This work shows the importance of grid adaptation for predicting important features of diffusing S-Duct flow fields and ultimately provides an improved prediction of total pressure at the AIP.

II. FUN3D Flow Solver

FUN3D^{9,10} is a finite-volume Navier-Stokes solver in which the flow variables are stored at the vertices or nodes of the mesh (i.e., node-centered). FUN3D solves the equations on mixed-element grids of tetrahedra, prisms, pyramids, and hexahedra. The code also supports two-dimensional structured (regular) grids and irregular grids composed of arbitrary mixtures of triangles and quadrilaterals. For tetrahedral meshes, the

full viscous fluxes are discretized using a finite-volume formulation in which the required velocity gradients on the dual faces are computed using the Green-Gauss theorem. On tetrahedral meshes this is equivalent to a Galerkin type approximation. For nontetrahedral meshes, the same Green-Gauss approach can lead to odd-even decoupling; a pure edge-based approach can be used, but yields only approximate viscous terms. Thus for nontetrahedral meshes, the edge-based gradients are combined with Green-Gauss gradients, which improves the h -ellipticity of the operator and allows the complete viscous stresses to be evaluated.¹¹ This formulation results in a discretization of the full Navier-Stokes equations.

At interfaces between neighboring control volumes, the inviscid fluxes are computed using an approximate Riemann solver based on values on either side of the interface. While FUN3D includes several convective flux schemes, Roe's flux difference splitting¹² is used in the current study. For second-order accuracy, interface values are obtained via extrapolation of control volume centroidal values based on gradients computed at mesh vertices by using an unweighted least-squares technique. FUN3D also includes a number of flux reconstruction limiters, but none were used in this study.

The solution at each time-step is updated with a backwards Euler time-integration scheme. At each time step, the linear system of equations is approximately solved with either a multicolor point-implicit technique or an implicit-line relaxation scheme.¹³ Local time-step scaling is employed to accelerate convergence to steady state. For turbulent flows, several models are available within FUN3D. Menter's two-equation SST turbulence model¹⁴ is used for results computed on the workshop-supplied grids; however, only the loosely coupled Spalart-Allmaras model¹⁵ is supported by the adjoint solver used in this study.

III. Output-Based Grid Adaptation

A common technique that aids in reducing numerical error is by changing the mesh in response to the developing flow solution and commonly referred to as adaptive mesh refinement. AMR techniques encompass a variety of different implementations. For example, feature-based adaptation increases mesh resolution where a variable of some characteristic feature in the solution is determined to be larger than average. An alternative method to feature-based adaptation is an output-based (adjoint) method that constructs an error estimate to improve the calculation of a specific engineering cost function, such as stagnation pressure and engine inflow distortion. The discrete adjoint formulation of the governing flow equations has been developed to provide sensitivity derivatives of output functionals to design variables. These adjoint equations are able to also provide a linear relationship between a distribution of local truncation error estimates and a particular output function. Therefore, the output-based grid adaptation method requires solution of both the governing flow equations and corresponding discrete adjoint equations.^{16–18}

The linear adjoint equations are solved in FUN3D with a dual-consistent time-marching method.¹³ The flow field adjoint equations are solved in an exact dual manner, which ultimately guarantees an asymptotic convergence rate that is identical to the primal problem and costate variables that are discretely adjoint at every iteration of the solution process. To improve adjoint iterative convergence and stability, a generalized conjugate residual (GCR) scheme¹⁹ is used with the standard multicolor point-implicit procedure as search directions.

The current output-based adaptation method implemented in FUN3D is based on the 2-D output-based error estimation adaptation scheme developed by Venditti and Darmofal,²⁰ which uses an embedded grid. This method has been expanded to 3-D²¹ and implemented in a parallel framework²² for use with FUN3D flow and adjoint solutions. The embedded grid necessary for the Venditti error estimator can be prohibitively large for 3-D problems (eight times the original grid), which can limit the problem size of the output adaptive method. To avoid this limitation, a single-grid error estimation procedure has been developed and compared to the embedded-grid procedure for Euler problems¹⁸ and turbulent simulations.²³ The current study uses the single-grid error estimator.

Venditti²⁴ developed a procedure to calculate a new grid spacing request from the adaptive indicator and a user-specified error tolerance. The anisotropy of mesh elements is based on a scaled Mach Hessian where the element size in the smallest spacing direction is dictated by the output-based spacing request.²⁴ This scaled Hessian is expressed as a metric, which is used by the adaptive grid mechanics. A constant-complexity scaling²⁵ can optionally be applied to this metric to allow the user to directly specify the size of the adapted grid. This size can be set to obtain an optimal grid that is computable with available resources.

In this study, the parallel grid mechanics described by Park and Darmofal²⁶ are used to modify the grid. The adaptation mechanics have only been implemented for tetrahedra. The local elemental operators, which

include parallel insertion and movement of nodes, collapsing and swapping cells, and anisotropic stretching are used to iteratively drive the edge lengths to unity in the scaled Hessian. The grid adaptation mechanics are unable to preserve the structure of anisotropic tetrahedra typically used near highly curved solid wall boundaries to resolve the viscous boundary layer region. The discretization in FUN3D is more accurate for semistructured right-angle tetrahedra in the boundary layer. To avoid these issues, the near wall boundary layer grid is frozen during the adaptation process. For this study, the grid is fixed an equivalent distance that equates to a y^+ of approximately 300, or the middle of the log layer.

IV. Propulsion Aerodynamics Workshop S-Duct Cases

The diffusing serpentine inlet modeled by workshop participants comes from the Inlet Flow Control and Prediction Technologies for Embedded Propulsion Systems (IFCPT) NASA technical report.²⁷ Test data was acquired at the Georgia Institute of Technology Transonic tunnel. Air was induced from ambient room conditions through the diffuser by creating low pressure downstream with a vacuum pump. Flow rate was controlled by running the pump at selected revolutions per minute (RPM) while measured with a calibrated Mass Flow Plug (MFP). The test case modeled the bellmouth contraction, upstream adapter section, IFCPT S-Duct, AIP housing, and 5-diameter extension as depicted in Fig. 1.

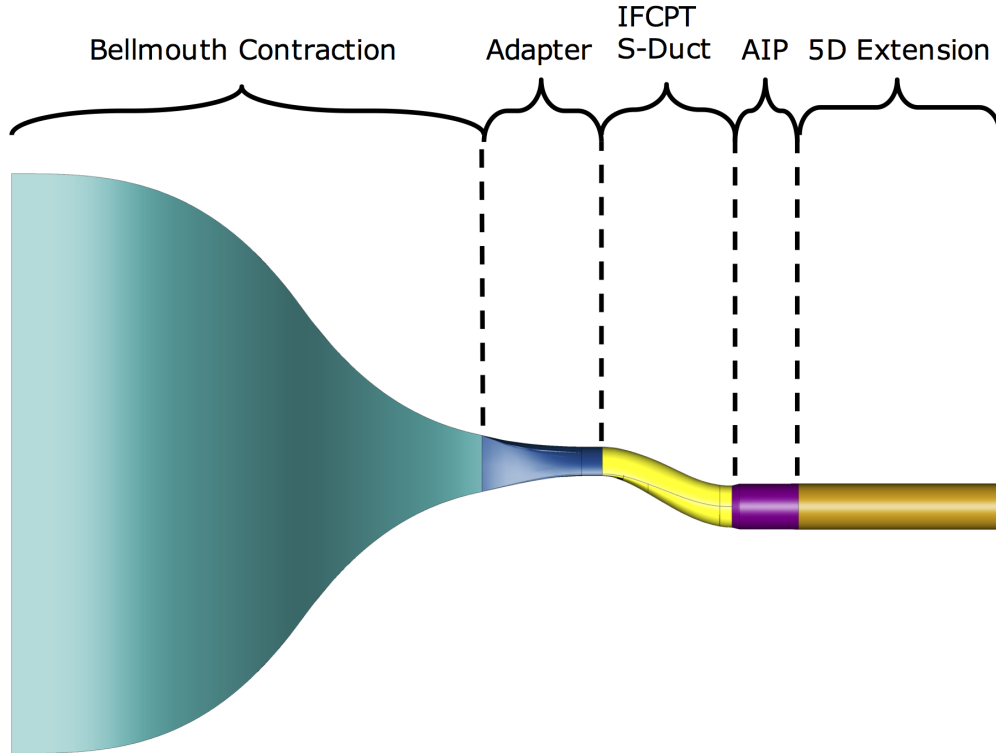
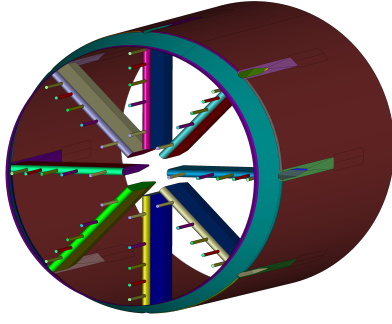


Figure 1: Components of the IFCPT S-Duct.

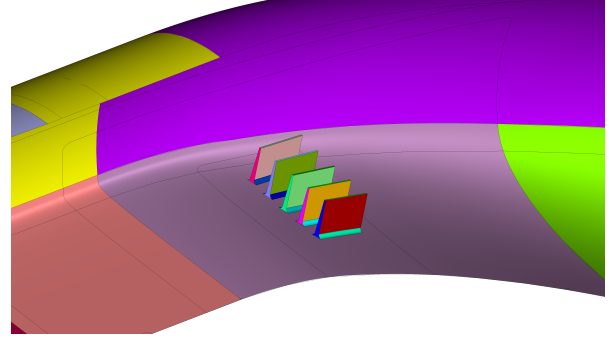
The AIP diameter (D) measures 5 inches, is offset $1.09(D)$ in the vertical direction, and has a length-to-diameter ratio (L/D) of 3.106. The model has a $5D$ extension added in order to impose a downstream constant pressure or mass flow boundary condition.

For the workshop, three separate S-Duct configurations and a set of four flow conditions were defined for participants to evaluate. In addition to the baseline inlet configuration, a second configuration modeled the S-Duct with 40-probe AIP instrumentation hardware while a third configuration incorporated a set of flow control devices used to induce flow separation in the offset diffuser's adverse pressure gradient turn. These two inlet configurations are illustrated in Fig. 2 on the next page.

Flow conditions provided for workshop participants to run are listed in Table 1 on the following page. The first two in the list correspond to conditions reported for the baseline S-Duct and S-Duct with AIP. The



(a) AIP Rake & Probe Instrumentation



(b) S-Duct with Flow Control Vanes

Figure 2: AIP instrumentation and flow control vanes were modeled in separate configurations to determine their influence on inlet performance metrics.

remaining two are provided for the case with flow control vanes. For this study, flow condition 1 is used for the baseline S-Duct and S-Duct with AIP instrumentation configurations while flow condition 3 is reserved for the S-Duct with passive flow control vanes case.

Table 1: Flow conditions for S-Duct results provided to PAW participants.

Flow Condition	AIP Mach Number	Total Pressure (lb/ft^2)	Total Temperature ($^{\circ}R$)	Mass Flow (lbm/sec)
1	0.6294	2072.9808	529.11	5.5322
2	0.5536	2072.9808	528.75	5.1407
3	0.6247	2072.9808	528.75	5.1407
4	0.5514	2072.9808	528.39	5.0726

There was a discrepancy with how mass flow rate values in Table 1 were reported by the test and how they were used by PAW03 participants. The test values were computed by using static and total pressure measurements to compute a Mach number as in Eq. (1).

$$M_2 = \frac{2}{(\gamma - 1)} \left[\left(\frac{P_{T2_{avg}}}{P_{2_{avg}}} \right)^{(\gamma - 1)/\gamma} \right]^{1/2} \quad (1)$$

Using this computed value for Mach number at the AIP with the AIP cross-sectional area (radius of 2.5 inches), the mass flow rate values were calculated as in Eq. (2).

$$W_2 = \frac{A_2 M_2 P_{T2_{avg}}}{\sqrt{\frac{RT_{T0}}{\gamma}}} \left[\frac{1 + (\gamma - 1)}{2} M_2^2 \right]^{\frac{(\gamma + 1)}{(2 - 2\gamma)}} \quad (2)$$

However, most CFD codes don't implement or automate prescribing mass flow at exit boundaries in this way; so some discrepancy exists between the reported test mass flow values and the mass flow used by workshop participants. Given this mismatch, some variance between computed values for total pressure recovery and test data is expected. Additionally, two AIP rakes were used in testing, and the rake geometry provided by PAW03 was not used at the specific test points corresponding to flow conditions listed in Table 1. Some slight differences between the two rakes exist that could potentially cause some additional variation between test and numerical results.

A comparison of workshop-supplied grids is shown in Table 2 on the next page. Solutions computed using these grids and FUN3D are employed to compare output-based grid adapted results prepared in this study with test data. For the baseline S-Duct configuration both structured/hexahedral and mixed-element unstructured grids were provided. For both the S-Duct with AIP and S-Duct with flow control vanes cases, only mixed-element unstructured grids were supplied. All of the grids in Table 2 on the following page are

half-symmetry meshes with the exception of the S-Duct with AIP grids, which use full-symmetry. A more complete overview of the mesh generation techniques used in creating the workshop-supplied grids is given by Winkler and Davis.⁶

Table 2: Set of standard workshop-supplied S-Duct meshes.

Mesh Configuration	Mesh Type	Number of Cells ($\times 10^6$)	Number of Nodes ($\times 10^6$)
Baseline S-Duct	Structured Coarse	3.30	3.49
	Structured Medium	10.29	10.70
	Structured Fine	19.95	20.58
	Unstructured Coarse	3.01	1.12
	Unstructured Medium	7.30	2.56
	Unstructured Fine	11.21	4.24
	Unstructured Fine 2	20.52	7.89
	Unstructured Fine 3	102.97	32.97
S-Duct with AIP	Unstructured Coarse	22.04	12.45
	Unstructured Medium	37.08	18.54
	Unstructured Fine	51.86	25.92
S-Duct with Vanes	Unstructured Coarse	4.26	2.32
	Unstructured Medium	10.37	5.02
	Unstructured Fine	20.84	8.98

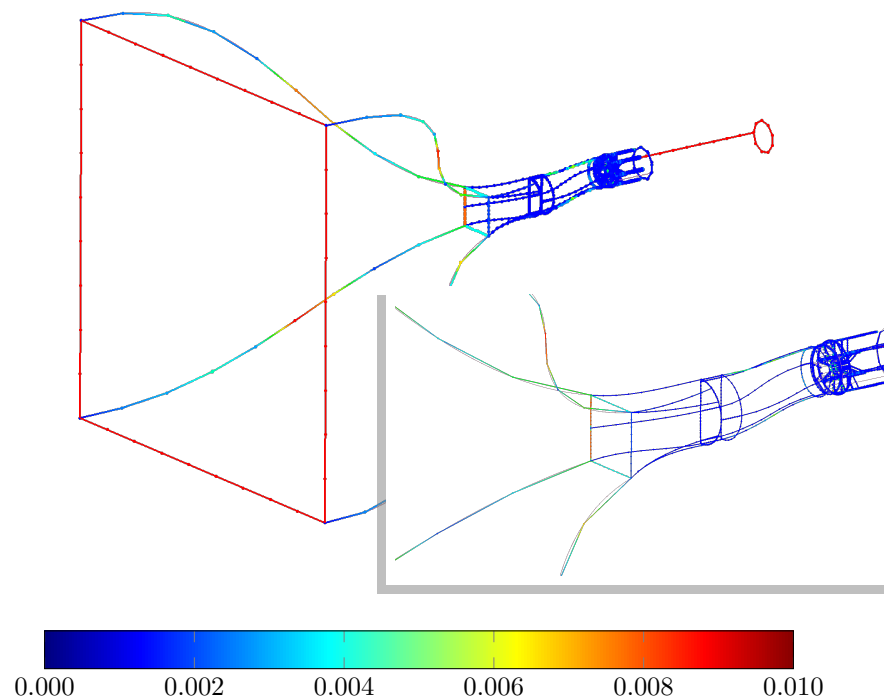


Figure 3: Boundary Proximity measurements of the geometry model for the S-Duct with AIP instrumentation show some small gaps between adjacent surfaces ranging between 0.007 to 0.009 inches at the bellmouth and adapter interface.

Initial grids used for output-based grid adaptation were created using the Pointwise[®] mesh generation software. Geometry processing was performed on a set of workshop-supplied geometry models provided in the form of IGES files.²⁸ After importing these geometry files into Pointwise, watertight solid models²⁹ were created using surface edge tolerances less than the smallest required mesh spacing as illustrated in Fig. 3.

Single watertight solid models for each inlet configuration were created in Pointwise by using the bellmouth adapter, IFCPT S-Duct, AIP, and 5D extension surfaces with a maximum edge tolerance of 0.0091 inches. After solid model assembly was completed, each model was split along a constant $y = 0$ plane to leverage model symmetry and reduce the initial grid size. Further geometry processing involved defining regions within each solid model where additional surface meshing control was desired or hard feature edges existed. Regions such as these, referred to as quilts,²⁹ are illustrated for the baseline IFCPT S-Duct after quilt assembly has been completed in Fig. 4. In Pointwise, each quilt will be meshed using a single 2-D surface grid entity referred to as a domain. An initial triangulated surface mesh with average Δs grid spacing varying between 0.75 inches in the bellmouth to 0.25 inches in the S-Duct and 5D extension was created. Additional isotropic grid refinement with average Δs spacing of 0.025 inches was used to add resolution in regions near the AIP instrumentation and flow control vanes for the S-Duct with AIP and S-Duct with flow control vanes cases, respectively.

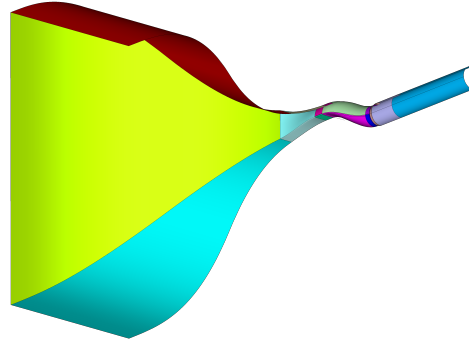


Figure 4: The surface mesh topology for the IFCPT S-Duct is shown after quilt assembly.

Given that the grid adaptation mechanics in FUN3D suffer some robustness problems when performing highly anisotropic adaptation near curved boundaries, coupled with the desire to adequately resolve the viscous boundary layer, four layers of prisms were extruded from the triangulated surface meshes by using an algebraic extrusion technique with optimization-based smoothing.³⁰ An initial wall normal cell height was specified using a $y^+ = 1$ distance of 9.11×10^5 inches, which was determined to be the smallest spacing required of the flow conditions listed in Table 1 on page 5. A geometric growth rate factor of 1.2 was applied as prism layers were marched normal to wall boundaries. From the extent of this prism extrusion, an anisotropic tetrahedral extrusion (T-Rex) advancing layer technique³¹ was employed to advance right-angled tetrahedra to isotropy by using the adjacent normal cell height from the last extruded prism layer and constant 1.2 growth factor. A comparison of grid sizes for these initial meshes along with their reported maximum cell skewness is shown in Table 3.

Table 3: Comparison of initial grids used in output-based mesh adaptation.

Case	Number of Cells ($\times 10^6$)	Number of Nodes ($\times 10^6$)	Maximum Included Angle ($^\circ$)
Baseline S-Duct	5.552	1.032	160.085
S-Duct with AIP	12.825	2.557	165.801
S-Duct with Vanes	9.311	1.733	169.263

A y -symmetry boundary condition was applied to all points lying along a constant $y = 0$ plane. A prescribed mass outflow boundary condition, where the static pressure is varied to match a user-specified target mass flow value, was applied to points along the exit of the 5D extension. Constant total pressure and total temperature conditions were prescribed at the bellmouth inlet. All points constrained to wall boundaries were set to an adiabatic, no-slip condition. Separate initial conditions for the x -component of velocity were applied to flow within the bellmouth contraction and flow downstream due to the large change in cross-sectional area.

V. Results

Steady-state Reynolds-averaged Navier-Stokes solutions for each of the structured/hexahedral and mixed-element unstructured workshop-supplied grids were computed using FUN3D to compare with solutions computed by using an output-based mesh adaptation approach. Menter's two-equation SST turbulence model was used instead of the single-equation SA model that was used in computing the output-based grid adaptation solutions due to limited turbulence modeling support in FUN3D's adjoint solver.

Contours of Mach number are shown for the workshop-supplied grids in Fig. 5 from solutions on the finest grid refinement level provided. A large change in the cross-sectional area in the vicinity of the AIP instrumentation hardware causes flow to separate and propagate to the exit boundary in all but the S-Duct with AIP configurations. This issue emphasizes the importance of either modeling the AIP instrumentation during numerical experiments, or modifying the inlet's Inner Mold Line (IML) to maintain consistency in the cross-sectional area distribution between numerical and test configurations.

Fig. 6 on the following page shows contours of total pressure recovery plotted at the AIP for each of the workshop-supplied grids for the baseline S-Duct and S-Duct with AIP cases. The total pressure recovery patterns show a low pressure region located at the twelve o'clock position due to the flow separation formed in both coarser structured/hexahedral and mixed-element grids. This is an artifact of cell volumes neighboring the separated region being too large; and as the mesh is refined further, the low pressure region disappears. As one would expect, this separation bubble doesn't appear at all in the S-Duct with AIP cases, and further demonstrates the importance of including all influential geometry components when comparing numerical and empirical results.

Total pressure recovery values reported in Fig. 6 on the next page are computed by surveying total pressure at prescribed x -, y -, and z -locations corresponding to the centers of each AIP rake probe. In the case of the S-Duct with AIP, these x -, y -, and z -coordinates are boundary points instead of points within the volume. An average over the 40 total pressure values is then computed, and the result is normalized by freestream total pressure. The x -, y -, and z -coordinates aren't necessarily collocated with grid points; so some interpolation between neighboring points is done by the solver. Computed total pressure recovery values for the cases in which the AIP instrumentation is not modeled are noticeably higher than the given test value for flow condition 1 of $P_{T2}/P_{T0} = 0.9784$. Computed total pressure recovery is higher than the reported experimental

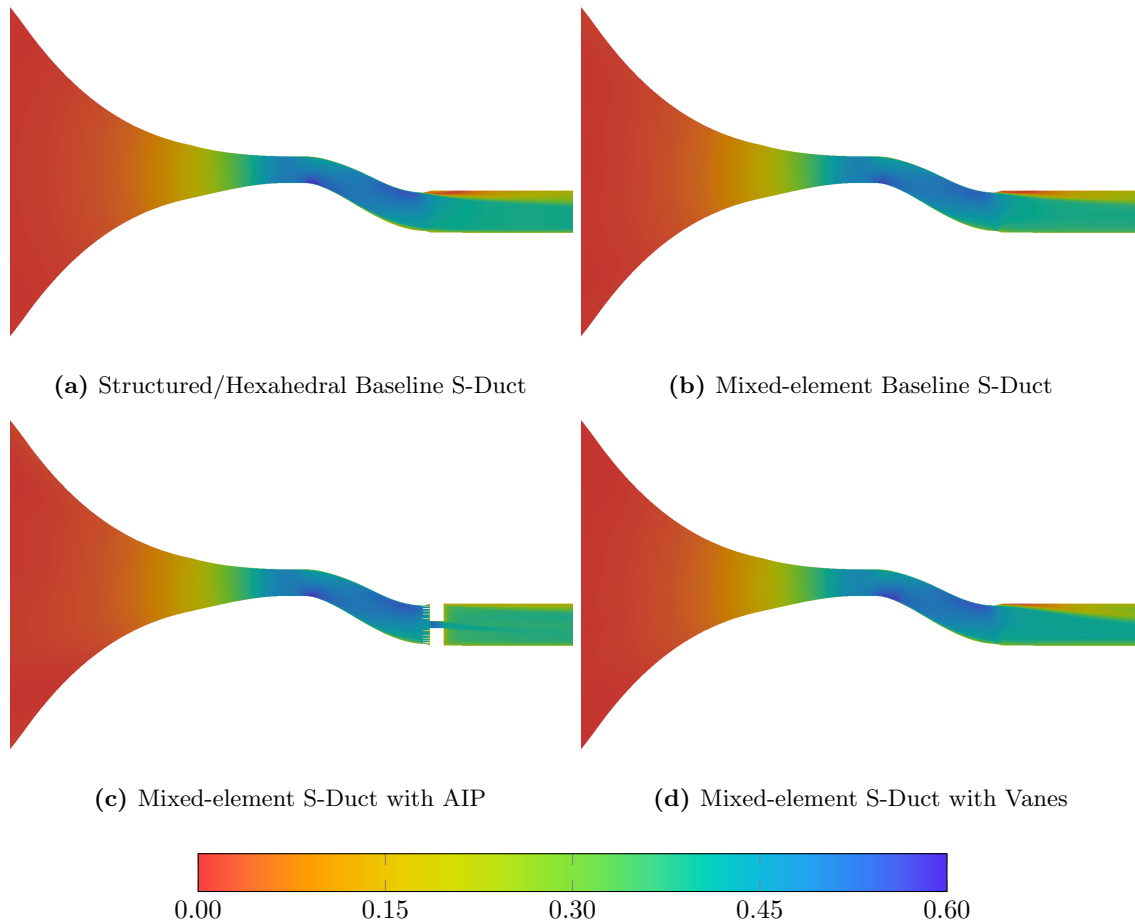
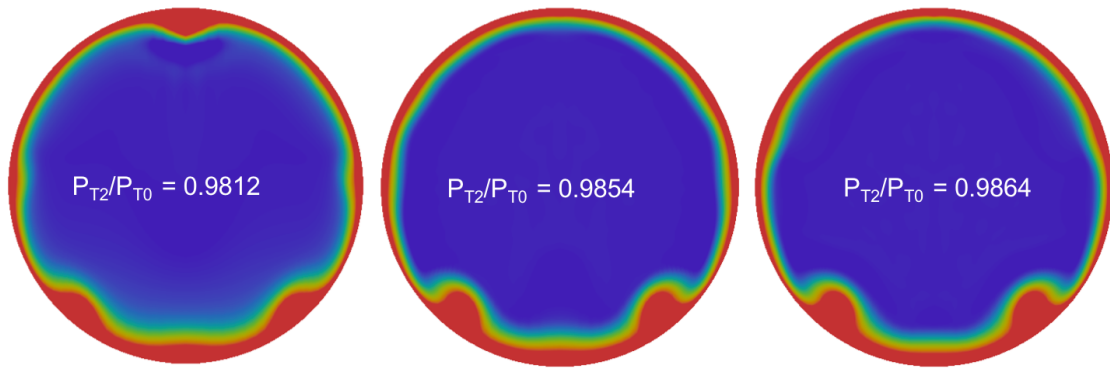
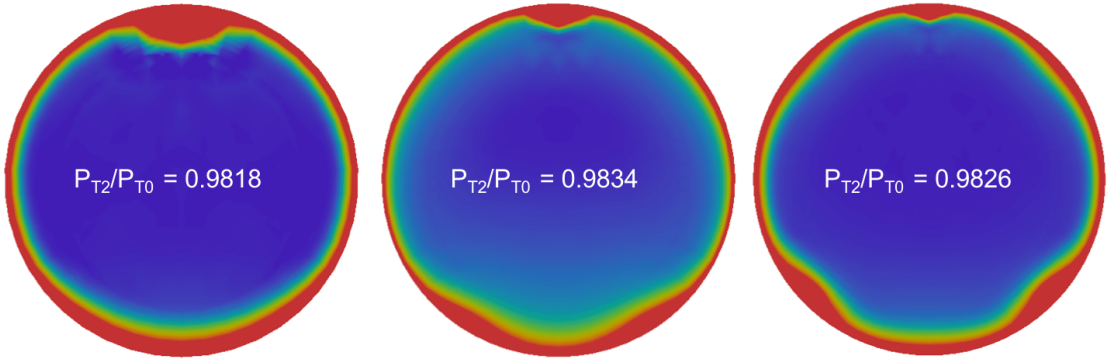


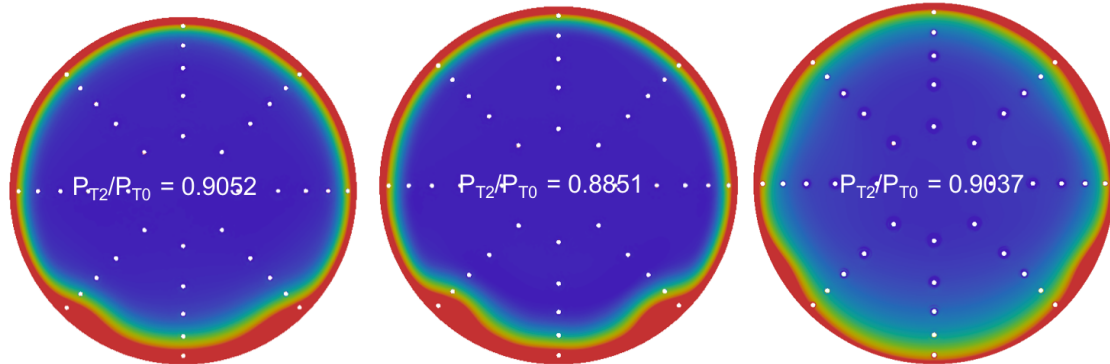
Figure 5: Mach contours plotted at a constant $y = 0$ plane show a localized separation region immediately downstream of the AIP in the absence of AIP rake instrumentation.



(a) Structured/Hexahedral Baseline S-Duct



(b) Mixed-element Baseline S-Duct



(c) Mixed-element S-Duct with AIP

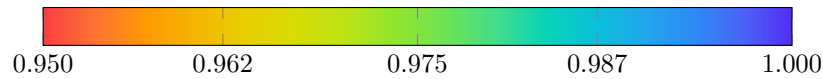


Figure 6: Total pressure recovery (P_{T2}/P_{T0}) contours plotted at the AIP for the various S-Duct configurations. Coarse, medium and fine workshop-supplied grids are shown from left to right for each configuration.

value primarily as a result of not modeling the total pressure loss associated with the AIP rake assembly. However, there are some other possible factors that contribute to the difference between computed and empirical values for each of these cases. For example, some slight variation exists between the prescribed mass flow rate in computed results, the mass flow rate surveyed at the AIP, and mass flow rate reported from the test. Even small changes in mass flow rate can directly influence total pressure recovery surveyed at the AIP. To circumvent this issue, practitioners typically simulate a number of conditions while varying the mass flow prescribed at the exit boundary to evaluate the inlet over a range of conditions. The last source of error

is due to the discretization error in the functional value. When one observes the difference (7.5% in the case of the finest workshop-supplied grid) in total pressure recovery between the S-Duct with AIP case and the nominal test result, this error can be a considerable component of the overall error in the computed results that output-based mesh adaptation helps resolve.

Using the initial grids described in Section IV, 10 adaptation cycles are run for each inlet configuration in which both flow and adjoint solvers are run, an error estimate of total pressure at the AIP is evaluated, and the grid adapted in response. A constant $y = 0.01$ inch cut of the initial and final adapted meshes for each case is shown in Fig. 7. For each case, a constant-complexity-scaling factor was applied and linearly varied over the course of 10 adaptation cycles from $N/2$ to 10.5×10^6 to drive adaptation on coarser grids initially and limit the optimal grid size to something that would fit within available computing resources. This adaptation factor is plotted against adaptation cycle in Fig. 8 on the next page. The ratio of the number of nodes to the complexity is near 2, which is expected by theory²⁵ and numerical experiments.³²

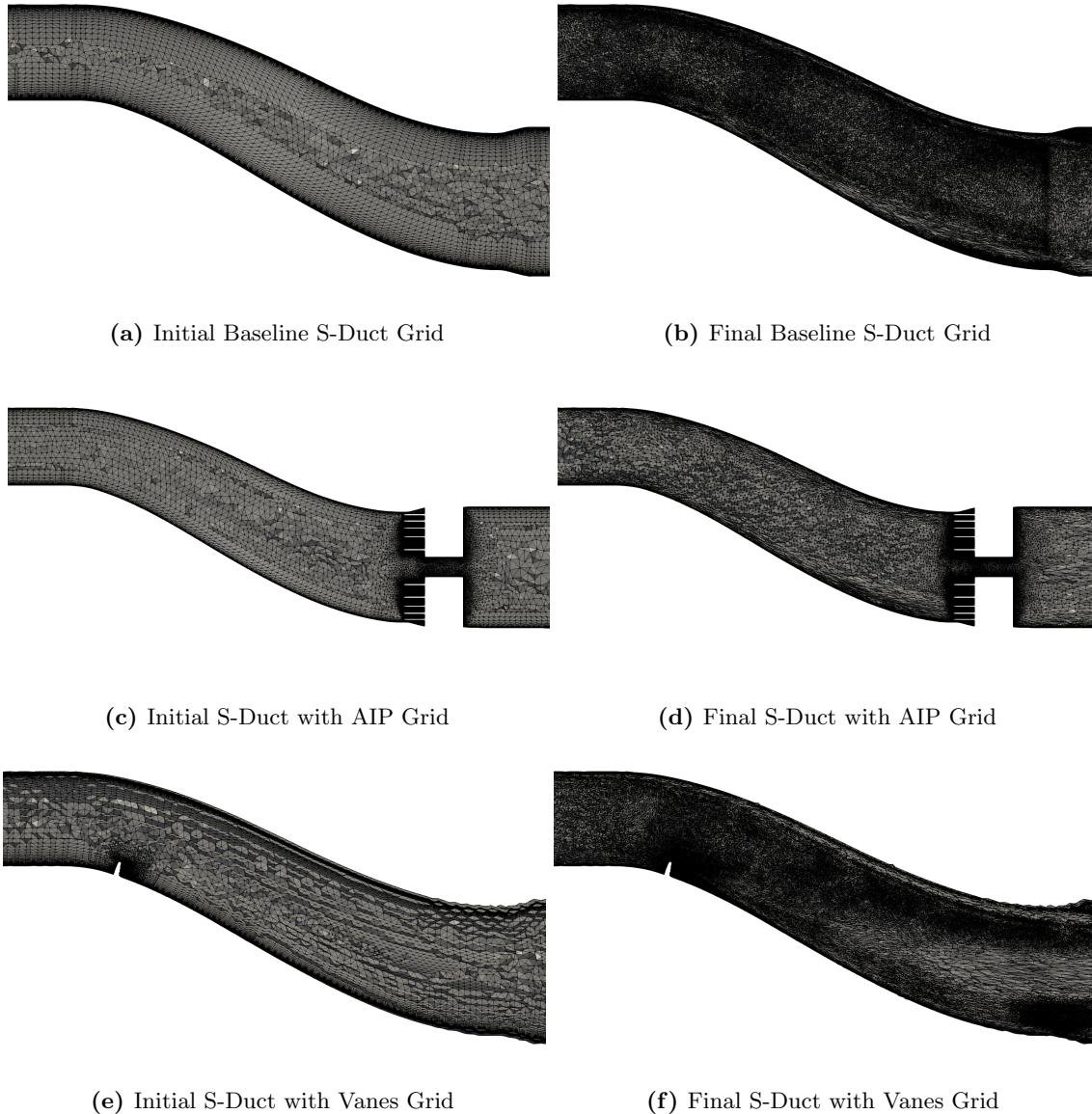


Figure 7: Comparison of initial and final adapted grids in the vicinity of the AIP for each S-Duct case.

Table 4 on page 12 lists total pressure recovery, mass flow, and steady-state distortion values from computed output-based mesh adapted solutions for each of the three cases. Here DPCP and DPRP are the circumferential and radial distortion intensity, respectively. The circumferential distortion intensity describes

the magnitude of the pressure defect for each ring of the AIP rake assembly, and is calculated by Eq. (3).

$$\text{DPCP}_i = \left(\frac{\text{PAV} - \text{PAVLOW}}{\text{PAV}} \right)_i \quad (3)$$

Here PAV is the ring-average pressure, PAVLOW is an average over any probes within a given ring that are below the ring average pressure, and i is the ring number.

The radial distortion intensity describes the difference between ring-average pressure and face-average pressure for each ring. Both positive and negative values of radial intensity are considered where positive values represent an average ring pressure that is below the face average pressure. DPCP and DPRP values ranging from 1 to 5 in Table 4 on the next page correspond to ring averages beginning with the innermost ring, or hub, and proceeding radially outward towards the outermost ring, or tip.

Mesh independence for the total pressure recovery functional was evaluated for both solutions computed on workshop-supplied and output-based mesh adapted grids. Results are shown in Fig. 9 on page 13. Along the abscissa, a substitute for the square of the characteristic grid spacing is plotted, where N is the number of grid nodes within a given mesh. For a 3-D problem, the characteristic grid length can be represented as $N^{1/3}$ per Roache.³³ It is not apparent that an asymptotic range is being approached as the mesh is refined for any of the workshop-supplied grids. This suggests that additional grid refinement may be needed. Formally, for a second-order scheme, there is a linear change in error versus the square of grid spacing for a consistently refined set of meshes.

A linear slope is an indication of the order of accuracy for a simulation. Particularly for the set of workshop-supplied grids, a linear trend is difficult to discern as the meshes for each configuration are refined. This nonlinearity may be due to irregular grid refinement, or additional features being resolved within the flow as the mesh is systematically refined.

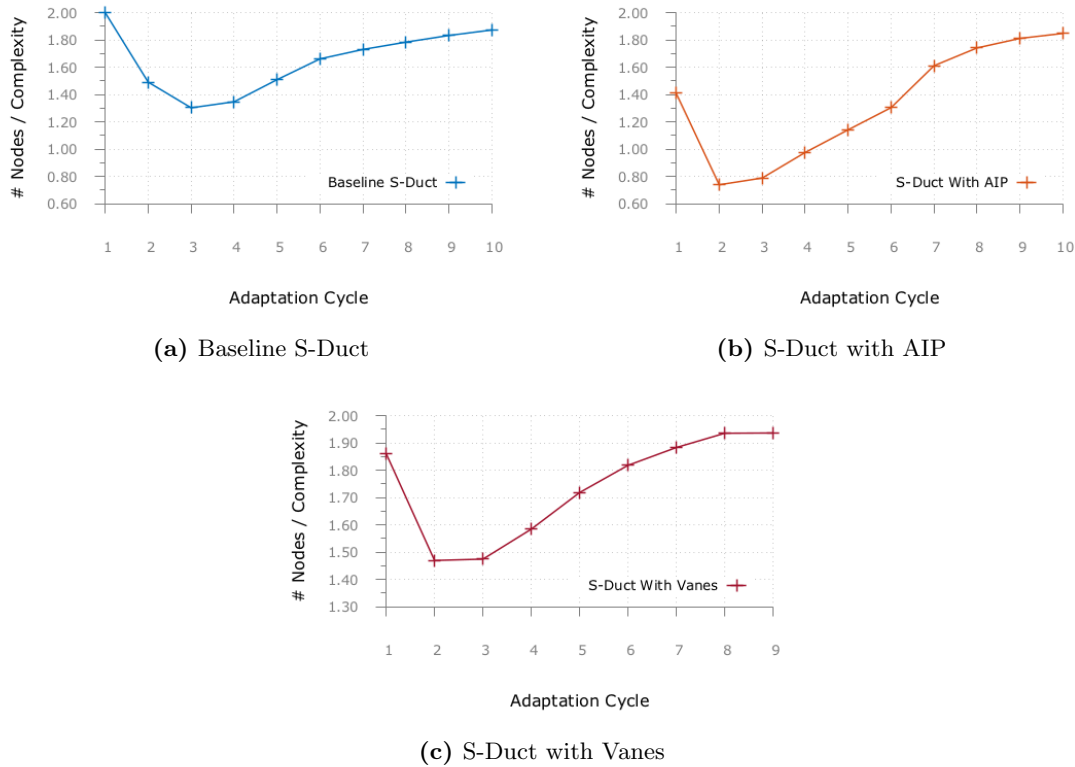


Figure 8: Complexity-scaling factor plotted versus adaptation cycle shows the adaptation factor approaches an asymptotic value of 2 in each case.

The NASA IFCPT report²⁷ indicates total pressure recovery for flow conditions 1 and 3 as $P_{T2}/P_{T0} = 0.9784$ and $P_{T2}/P_{T0} = 0.9638$, respectively. Results for the baseline S-Duct show a 0.65% disparity in total pressure recovery between this test value and the value listed in Table 4 on the next page computed using output-based

Table 4: Summary of computed results from output-based mesh-adaptation.

	Baseline S-Duct	S-Duct with AIP	S-Duct with Vanes
P_{T2}/P_{T0}	0.9849	0.9781	0.9795
W_2 (lbm/s)	5.5292	5.5236	5.4345
DPCP1	0.0000	0.0718	0.0000
DPCP2	0.0000	0.0198	0.0291
DPCP3	0.0000	0.0809	0.0332
DPCP4	0.0199	0.0854	0.0286
DPCP5	0.0143	0.0740	0.0133
DPRP1	-0.0139	-0.0119	-0.0199
DPRP2	-0.0139	0.0739	-0.0005
DPRP3	-0.0139	-0.0499	0.0022
DPRP4	0.0012	-0.0083	0.0015
DPRP5	0.0405	-0.0039	0.0168
DPCP _{AVG}	0.0069	0.0664	0.0209

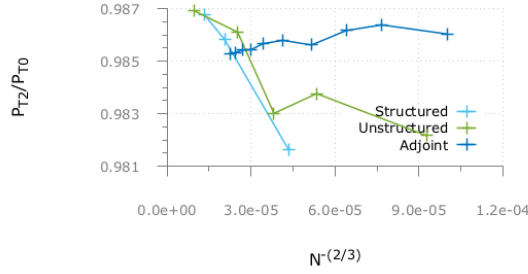
mesh adaptation. Similarly, a 1.57% difference exists between the reported test value and the output-based mesh adaptation result for the S-Duct with Vanes case. This is primarily attributed to not resolving the pressure loss due to the AIP rake assembly and introducing a localized flow separation as a result of the change in cross-sectional area distribution in both cases. Given that the AIP instrumentation is not being modeled in either of these cases, and it has a significant influence on the functional being evaluated, an estimate for what this value would be can be derived.

Assuming second-order accuracy, one can extrapolate the output-based mesh adapted results to $N^{-(2/3)} = 0$ to estimate an exact value for P_{T2}/P_{T0} given an infinitely refined mesh. From the baseline S-Duct case, this extrapolated value of $N^{-(2/3)} = 0$ is $P_{T2}/P_{T0} = 0.9851$. From this, the percent difference in the computed functional value for the output-based mesh adaptation case is only 0.02%. Because the results computed on the workshop-supplied grids were run using a different turbulence model, they aren't expected to have the same $N^{-(2/3)} = 0$ extrapolation. Performing similar extrapolations for the structured/hexahedral and unstructured mixed-element grids separately yields estimates for an exact total pressure recovery value as $P_{T2}/P_{T0} = 0.9892$ and $P_{T2}/P_{T0} = 0.9868$, respectively. Similarly, for the structured/hexahedral workshop-supplied grids the percent difference in the computed functional value is 0.28%; whereas, for the unstructured mixed-element meshes it is 0.42%. These results for the baseline S-Duct highlight the advantage of output-based, off-body mesh adaptation in predicting the functional value.

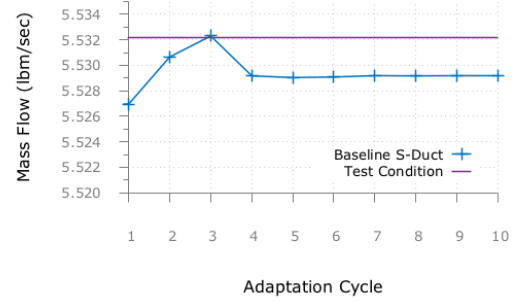
For the S-Duct with Vanes case, extrapolating to $N^{-(2/3)} = 0$ for the adapted grid results yields $P_{T2}/P_{T0} = 0.9790$, which results in a 0.05% difference between computed and exact values. For the workshop-supplied grids, the estimated exact value from extrapolation is $P_{T2}/P_{T0} = 0.9858$. The computed value for total pressure recovery on the finest workshop-supplied grid level for the S-Duct with Vanes case was $P_{T2}/P_{T0} = 0.9840$, which results in a change of 0.18%. For both S-Duct configurations the prediction of the functional value is considerably improved when using output-based mesh adaptation.

The S-Duct with AIP case allows for the most direct comparisons between the reported test value and computed results in total pressure recovery. For this particular configuration, there is only a difference of 0.054% between measured and prescribed W_2 . Only a 0.03% difference exists between the experimental pressure recovery reported ($P_{T2}/P_{T0} = 0.9784$) and the output-based mesh adaptation computed value ($P_{T2}/P_{T0} = 0.9781$). This compares with a 7.5% difference between the experimental value and the finest grid refinement level from the workshop-supplied grid ($P_{T2}/P_{T0} = 0.9037$).

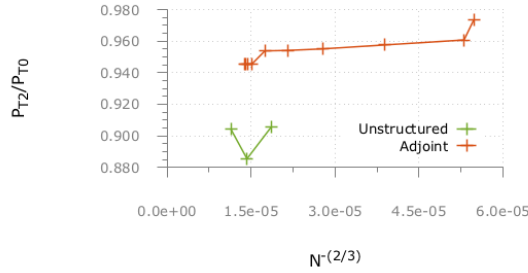
Although steady-state distortion parameters were not the focus of this study, an engine inflow distortion cost function has been recently added to FUN3D.³⁴ The experimental DPCP_{AVG} steady-state distortion value reported for flow condition 1 was 0.058. Comparing this value with output-based mesh adaptation using total pressure as the functional yields a difference of 14.4%. This demonstrates how an optimal grid for one functional isn't necessarily suitable for accurate prediction of another engineering cost function.



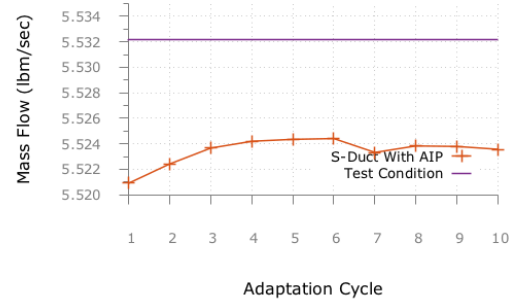
(a) Baseline S-Duct P_{T2}/P_{T0} convergence



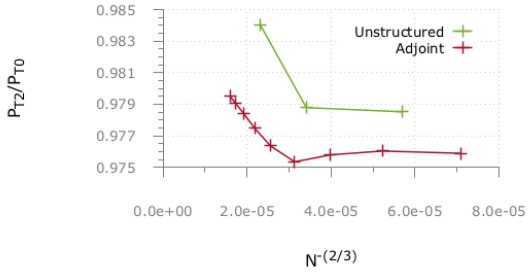
(b) Baseline S-Duct W_2 convergence



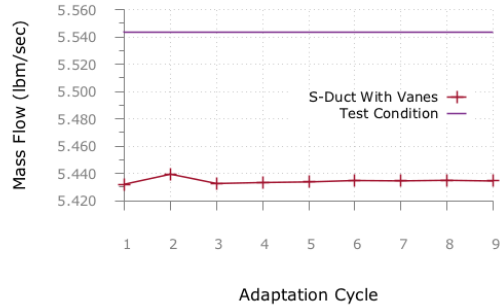
(c) S-Duct with AIP P_{T2}/P_{T0} convergence



(d) S-Duct with AIP W_2 convergence



(e) S-Duct with Vanes P_{T2}/P_{T0} convergence



(f) S-Duct with Vanes W_2 convergence

Figure 9: Comparison of convergence for the computed functional, P_{T2}/P_{T0} , and corresponding mass flow rate, W_2 on adapted and workshop-supplied grids.

VI. Conclusions

Contributions of the unstructured Reynolds-averaged Navier-Stokes code FUN3D to the 3rd AIAA CFD Propulsion Aerodynamics Workshop were described, and detailed comparisons were made with experimental data on three separate diffusing IFCPT S-Duct configurations. A grid convergence study was performed on workshop-supplied grids that showed additional grid refinement was likely needed due to nonlinear convergence behavior where total pressure recovery was not observed approaching an asymptotic range. Output-based, off-body grid adaptation was applied to each of the three S-Duct configurations to explore automated grid refinement and improved CFD prediction of total pressure recovery surveyed at the AIP. The computations with output-based grids follow the latest innovations in CFD applied to complex internal flow applications and represent active development at the leading edge of CFD capabilities.

The results of the current computational study point to the need for proper representation of all influential geometry components. Drawing comparisons between experimental and numerical values is particularly

challenging when influential components such as the AIP rake assembly are omitted. In the case where the AIP rake assembly was included, output-based, off-body grid adaptation results compared very favorably with experimental data—much more so than results obtained using the workshop-supplied grids that did not include the AIP rake assembly. Another compounding effect involved correctly matching the computed mass flow rate through the inlet diffuser with the experimental values. Given the influence mass flow rate has on many propulsion aerodynamic performance metrics, accurately predicting the flow field at a single point can be especially challenging. Particular attention is needed to determine how mass flow rate is reported when used as a reference, and corrections should be applied to prescribed exit boundary conditions as needed. As a workaround, workshop participants could be encouraged to submit a set of results computed at various mass flow conditions for future workshops. Lastly, some additional work is needed to determine how best to survey total pressure—whether to survey the flow at single points as was done in the current study, compute an area-weighted average over each Kulite® pressure probe face, or something else.

A considerable improvement in accurately predicting total pressure recovery was observed when using output-based grid adaptation techniques versus the workshop supplied grids. The use of grid adaptation will undoubtedly be an important component in accurately predicting engineering metrics of importance in the future. The ability to automatically add grid resolution in areas of the flow field where it is needed removes the need for often time-consuming, human-driven mesh generation and economizes computational resources.³⁵

References

- ¹“3rd Propulsion Aerodynamics Workshop Mesh & Geometry Web Site,” <https://sites.google.com/site/paw03aiaa2016/mesh-and-geometr>, Accessed: Jan 2017.
- ²Delot, A. and Scharnhorst, R., “A Comparison of Several CFD Codes with Experimental Data in a Diffusing S-Duct,” 49th AIAA/SAE/ASEE Joint Propulsion Conference, AIAA Paper 2013–3796, San Jose, CA, July 2013.
- ³Thornock, R. L., “Propulsion Aerodynamic Workshop I: Comparison of Participant Analyses with Experimental Results for Convergent Conical Nozzle Flow Fields and Performance,” 49th AIAA/SAE/ASEE Joint Propulsion Conference, AIAA Paper 2013–3735, San Jose, CA, July 2013.
- ⁴Scharnhorst, R. and Delot, A., “Computational and Experimental Results for Flows in a Diffusing S-Duct without and with Flow Control Devices,” 51st AIAA/SAE/ASEE Joint Propulsion Conference, AIAA Paper 2015–3964, Orlando, FL, July 2015.
- ⁵Thornock, R. L. and Sokhey, J. S., “Propulsion Aerodynamic Workshop II: Participants’ Analyses of a Dual Separate Flow Reference Nozzle in Terms of Thrust and Flow Performance,” 52nd AIAA/SAE/ASEE Joint Propulsion Conference, AIAA Paper 2016–4503, Salt Lake City, UT, July 2016.
- ⁶Winkler, C. M. and Davis, Z. S., “Summary of the 3rd Propulsion Aerodynamics Workshop: S-duct Results,” 53rd AIAA/SAE/ASEE Joint Propulsion Conference, Atlanta, GA, July 2017.
- ⁷“Gas Turbine Engine Inlet Flow Distortion Guidelines,” SAE ARP 1420 Rev. C, Society of Automotive Engineers International, Warrendale, PA, April 2017.
- ⁸Biedron, R. T., Carlson, J.-R., Derlaga, J. M., Gnoffo, P. A., Hammond, D. P., Jones, W. T., Kleb, B., Lee-Rausch, E. M., Nielsen, E. J., Park, M. A., Rumsey, C. L., Thomas, J. L., and Wood, W. A., “FUN3D Manual: 13.1,” NASA/TM–2017–219580, NASA, Feb. 2017.
- ⁹Anderson, W. K. and Bonhaus, D. L., “An Implicit Upwind Algorithm for Computing Turbulent Flow on Unstructured Grids,” *Comp. & Fluids*, Vol. 23, No. 1, Jan. 1994, pp. 1–21.
- ¹⁰Anderson, W. K., Rausch, R. D., and Bonhaus, D. L., “Implicit/Multigrid Algorithm for Incompressible Turbulent Flows on Unstructured Grids,” *Journal of Computational Physics*, Vol. 128, No. 2, 1996, pp. 391–408, See also AIAA Paper 95–1740.
- ¹¹Diskin, B., Thomas, J. L., Nielsen, E. J., Nishikawa, H., and White, J. A., “Comparison of Node-Centered and Cell-Centered Unstructured Finite Volume Discretizations: Viscous Fluxes,” *AIAA Journal*, Vol. 48, No. 7, July 2010, pp. 1326–1338.
- ¹²Roe, P. L., “Approximate Riemann Solvers, Parameter Vectors, and Difference Schemes,” *Journal of Computational Physics*, Vol. 43, 1981, pp. 357–372.
- ¹³Nielsen, E. J., Lu, J., Park, M. A., and Darmofal, D. L., “An Implicit, Exact Dual Adjoint Solution Method for Turbulent Flows on Unstructured Grids,” *Computers and Fluids*, Vol. 33, No. 9, 2004, pp. 1131–1155.
- ¹⁴Menter, F. R., “Two-Equation Eddy-Viscosity Turbulence Models for Engineering Applications,” *AIAA Journal*, Vol. 32, No. 8, Aug. 1994, pp. 1598–1605.
- ¹⁵Spalart, P. and Allmaras, S. R., “A One-Equation Turbulence Model for Aerodynamic Flows,” *Recherche Aerospatiale*, Vol. 1, 1994, pp. 5–21.
- ¹⁶Nielsen, E. J., *Aerodynamic Design Sensitivities on an Unstructured Mesh Using the Navier-Stokes Equations and a Discrete Adjoint Formulation*, Ph.D. thesis, Virginia Polytechnic Institute and State University, Dec. 1998.
- ¹⁷Nielsen, E. J. and Anderson, W. K., “Recent Improvements in Aerodynamic Design Optimization on Unstructured Meshes,” *AIAA Journal*, Vol. 40, No. 6, 2002, pp. 1155–1163.
- ¹⁸Park, M. A., *Anisotropic Output-Based Adaptation with Tetrahedral Cut Cells for Compressible Flows*, Ph.D. thesis, Massachusetts Institute of Technology, Sept. 2008.

- ¹⁹Eisenstat, S. C., Elman, H. C., and Schultz, M. H., “Variational Iterative Methods for Nonsymmetric Systems of Linear Equations,” *SIAM Journal on Numerical Analysis*, Vol. 20, No. 2, April 1983, pp. 345–357.
- ²⁰Venditti, D. A. and Darmofal, D. L., “Grid Adaptation for Functional Outputs: Application to Two-Dimensional Inviscid Flows,” *Journal of Computational Physics*, Vol. 176, 2002, pp. 40–69.
- ²¹Park, M. A., “Three-Dimensional Turbulent RANS Adjoint-Based Error Correction,” *16th AIAA Computational Fluid Dynamics Conference*, AIAA Paper 2003–3849, Orlando, FL, June 2003.
- ²²Lee-Rausch, E. M., Park, M. A., Jones, W. T., Hammond, D. P., and Nielsen, E. J., “Application of a Parallel Adjoint-Based Error Estimation and Anisotropic Grid Adaptation for Three-Dimensional Aerospace Configurations,” *23rd AIAA Applied Aerodynamics Conference*, AIAA Paper 2005–4842, Toronto, Ontario Canada, June 2005.
- ²³Park, M. A., Lee-Rausch, E. M., and Rumsey, C. L., “FUN3D and CFL3D Computations for the First High Lift Prediction Workshop,” *49th AIAA Aerospace Sciences Meeting*, AIAA Paper 2011–936, Orlando, FL, Jan. 2011.
- ²⁴Venditti, D. A., *Grid Adaptation for Functional Outputs of Compressible Flow Simulations*, Ph.D. thesis, Massachusetts Institute of Technology, June 2002.
- ²⁵Loseille, A. and Alauzet, F., “Continuous Mesh Framework Part I: Well-Posed Continuous Interpolation Error,” *SIAM Journal on Numerical Analysis*, Vol. 49, No. 1, 2011, pp. 38–60.
- ²⁶Park, M. A. and Darmofal, D., “Parallel Anisotropic Tetrahedral Adaptation,” *46th AIAA Aerospace Sciences Meeting and Exhibit*, AIAA Paper 2008–917, Reno, NV, Jan. 2008.
- ²⁷McMillan, M. L., Mackie, S. A., Gissen, A., Vukasinovic, B., Lakebrink, M. T., Glezer, A., Mani, M., and Mace, J. L., “Inlet Flow Control and Prediction Technologies for Embedded Propulsion Systems,” NASA/CR—2011-217237, NASA, Dec. 2011.
- ²⁸Reed, K., “The Initial Graphics Exchange Specification (IGES),” NISTIR 4412, National Institute of Standards and Technology, 1991.
- ²⁹Steinbrenner, J. P., Wyman, N. J., and Chawner, J. R., “Fast Surface Meshing on Imperfect CAD Models,” *9th International Grid Conference*, New Orleans, LA, 2000.
- ³⁰Karman, S. L. and Remotigue, M. G., “Optimization-Based Smoothing for Extruded Meshes,” *54th AIAA Aerospace Sciences Meeting*, AIAA Paper 2016–1671, San Diego, CA, Jan. 2016.
- ³¹Steinbrenner, J. P. and Abelanet, J. P., “Anisotropic Tetrahedral Meshing Based on Surface Deformation Techniques,” *AIAA 45th Aerospace Sciences Meeting*, AIAA Paper 2007–0554, Reno, NV, Jan. 2007.
- ³²Loseille, A. and Alauzet, F., “Continuous Mesh Framework Part II: Validations and Applications,” *SIAM Journal on Numerical Analysis*, Vol. 49, No. 1, 2011, pp. 61–86.
- ³³Roache, P. J., *Verification and Validation in Computational Science and Engineering*, Hermosa Publishers, Albuquerque, NM, 1998.
- ³⁴Ordaz, I., Rallabhandi, S. K., Nielsen, E. J., and Diskin, B., “Mitigation of Engine Inlet Distortion through Adjoint-Based Design,” *23rd Computational Fluid Dynamics Conference*, Denver, CO, June 2017.
- ³⁵Slotnick, J., Khodadoust, A., Alonso, J., Darmofal, D., Gropp, W., Lurie, E., and Mavriplis, D., “CFD Vision 2030 Study: A Path to Revolutionary Computational Aerosciences,” NASA/CR–2014–218178, NASA, March 2014.